UCLA
UCLA Previously Published Works

Title

A unimorph nanocomposite dielectric elastomer for large out-of-plane actuation

Permalink

https://escholarship.org/uc/item/56p1f43w

Journal

Science Advances, 8(9)

ISSN

2375-2548

Authors

Pu, Junhong
Meng, Yuan
Xie, Zhixin
et al.

Publication Date

2022-03-04

DOI

10.1126/sciadv.abm6200

Peer reviewed

A unimorph nanocomposite dielectric elastomer for large out-of-plane actuation

Junhong Pu[1,2], Yuan Meng[1,*], Zhixin Xie[1], Zihang Peng[1], Jianghan Wu[1], Ye Shi[1], Roshan Plamthottam[1], Wei Yang[2,*], and Qibing Pei[1,*]

[1]Department of Materials Science and Engineering, Henry Samueli School of Engineering and Applied Science, University of California, Los Angeles, CA 90095, USA.

[2]College of Polymer Science and Engineering, State Key Laboratory of Polymer Materials Engineering, Sichuan University, Chengdu, Sichuan, 610065, China.

*Correspondence: qpei@seas.ucla.edu, ymeng5@ucla.edu, weiyang@scu.edu.cn

ABSTRACT

Dielectric elastomer actuators (DEAs) feature large, reversible in-plane deformation, and stacked DEA layers are used to produce large strokes in the thickness dimension. We introduce an electrophoretic process to concentrate boron nitride nanosheet dispersion in a dielectric elastomer precursor solution onto a designated electrode surface. The resulting unimorph nanocomposite dielectric elastomer (UNDE) has a seamless bilayer structure with 13 times of modulus difference. The UNDE can be actuated to large bending curvatures, with enhanced breakdown field strength and durability as compared to conventional nanocomposite dielectric elastomer (CNDE). Multiple UNDE units can be formed in a simple electrophoretic concentration process using patterned electrode areas. A disc-shaped actuator comprising 6 UNDE units outputs large bidirectional stroke up to 10 Hz. This actuator is used to demonstrate a high-speed lens motor capable of varying the focal length of a two-lens system by 40 times.

INTRODUCTION

Dielectric elastomers are a class of electroactive polymers that can efficiently transduce electromechanical energy(*1-3*). Dielectric elastomer actuators (DEAs) operate through an electrostatic stress mechanism in response to an applied voltage, and are characterized by their large strain and high energy density(*1*). DEAs have attracted tremendous interest in the past decade due to their extensive applications for artificial muscles(*3, 4*), soft robotics(*5, 6*), and haptics(*7, 8*).

Among the most studied dielectric elastomers, acrylic elastomers have been identified to exhibit the largest actuation strain(*1*), but this outstanding performance is overshadowed by the prestretch procedure involved during fabrication, which wanes over time due to stress relaxation(*9*). In addition, bulky rigid frames are required to support the prestretched film, which complicates the device structure and limits potential applications. Numerous efforts have been made to eliminate prestretch while retaining the featured actuation performance of acrylic elastomers. Dielectric elastomers produced by introducing a second interpenetrating polymer network(*10*) and chemical modification(*11, 12*) can achieve large actuation strains (> 100%) without prestretch. However, most of the non-prestretched dielectric elastomers work under relatively high driving fields and tend to have low field strengths. It is possible to enhance the dielectric constant of a material and effectively lower the driving field by blending high permittivity ceramics into the dielectric matrix(*13, 14*). However, many of these additives invariably increase the leakage current and lower the breakdown field strength, and a high filler loads (> 15 wt%) are usually required to see a considerable performance improvement(*15, 16*).

Conventional DEAs generate in-plane deformation which is difficult to outcouple and not the most practical mode of actuation. In order to produce large out-of-plane actuation that can be conveniently coupled for practical applications, such as haptic displays(*17*), soft grippers(*18*), and robot locomotion(*19*), various

actuator configurations have been proposed with non-prestretch dielectric materials. Stacked DEAs can enlarge the linear stroke in the thickness (z) direction. Multilayer devices comprising hundreds of stacked dielectric elastomer thin films have been reported to deliver millimeter-scale linear motion in the z-direction[4, 20, 21]. These stacking processes, however, often are extremely time-consuming and have low yield. Alternatively, dielectric elastomer films can also be attached to passive structures to generate out-of-plane actuation[22, 23]. While it is possible to use the DE material's inherent tackiness[24] and covalent bonds[25] to adhere to constraining layers, the two-part structures are often jeopardized by trapped air bubbles and delamination after repeated bending cycles, and the actuation is limited with non-linear bending deformation.

Here we introduce an electrophoretic approach followed by in-situ crosslinking for the fabrication of an interface-free unimorph nanocomposite dielectric elastomer (UNDE) comprised of locally concentrated boron nitride nanosheets (BNNS). The BNNS function as a passive structure that creates anisotropic stiffness along the z-direction, so that the UNDE film can bend in response to an applied electric field. The thin (~3.1 μm) and dense (~72 wt% of BNNS) BNNS-concentrated insulating layer also contributes to the breakdown strength enhancement of the UNDE. The electrophoretic process is highly programmable to produce multiple functional unimorph units in a disc-shaped monolithic DEA film via customized electrode patterning. This new multi-unit device structure converts synchronized individual bending actuations into linear displacement, and generates linear motions up to ±1.38 mm in the z-direction, which is 13 times the thickness of the DEA film. The actuation strain could be varied with the applied voltage, and shows no degradation with increasing frequency up to 10 Hz. This compact actuator can provide large linear actuation within a narrow space, and we demonstrated its use as a direct-drive lens motor for an optical zoom system to obtain large focal length variation at high speed.

RESULTS

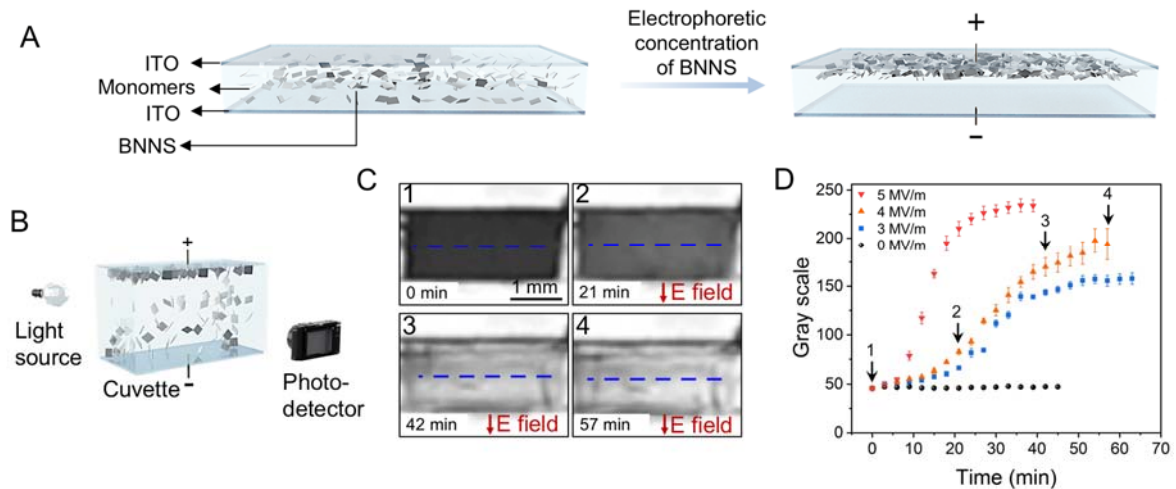**Fabrication of an UNDE film via electrophoretic concentration**

Fig. 1. Illustration of electrophoretic concentration process to create an UNDE film. (**A**) BNNS dispersed in a dielectric elastomer monomer solution are attracted to the positive electrode surface through an electrophoretic concentration process. (**B**) A setup to study the kinetics of the electrophoretic concentration process: a light source and a photodetector are placed on opposite sides of a cuvette chamber where the electrophoretic concentration of BNNS takes place. (**C**) Grayscale images of the cuvette chamber taken by the photodetector at specified elapsed time of the electrophoretic process. The electric field applied is 4 MV/m constant. (**D**) Recorded grayscale value versus electrophoretic time at the specified electric field. The grayscale

value is taken as the average value along the dashed line shown in Fig. 1C. Numbered arrows indicate the time the images in Fig. 1C.

A continuous UNDE film with highly concentrated BNNS on one surface was fabricated using the electrophoresis process shown in Fig. 1A. BNNS, a commonly used dielectric filler to enhance dielectric strength (*26*), were dispersed in a dielectric elastomer precursor to form a colloidal suspension (Fig. S1). The dispersion was injected between two parallel electrodes where a direct current (DC) electric field was applied. Since the BNNS was negatively charged(*27*), they were attracted to the surface of the positive electrode. After this electrophoretic concentration process, the precursor was cured via UV exposure. The resulting solid dielectric elastomer film comprised a layer of BNNS within one of its surface layers, forming a continuous bilayer structure.

Fig. 1B shows the optical setup used to monitor the BNNS electrophoretic concentration process. The process was imaged using a light beam that passes through the cuvette chamber where electrophoresis takes place (Fig. 1C). The grayscale images were used to monitor the BNNS concentration in the dispersion during electrophoresis(*28*). The temporal evolution of the midline between the two electrophoretic electrodes shown in Fig. 1D and Fig. S2 indicates a faster BNNS concentration toward the positive electrode and a more thorough depletion of BNNS in the bulk of the solution at higher electric fields. Electric fields larger than 5 MV/m increased the probability of dielectric breakdown of the liquid precursor. As a result, the BNNS electrophoretic concentration was performed at 5 MV/m for 40 min to make the continuous UNDE below.

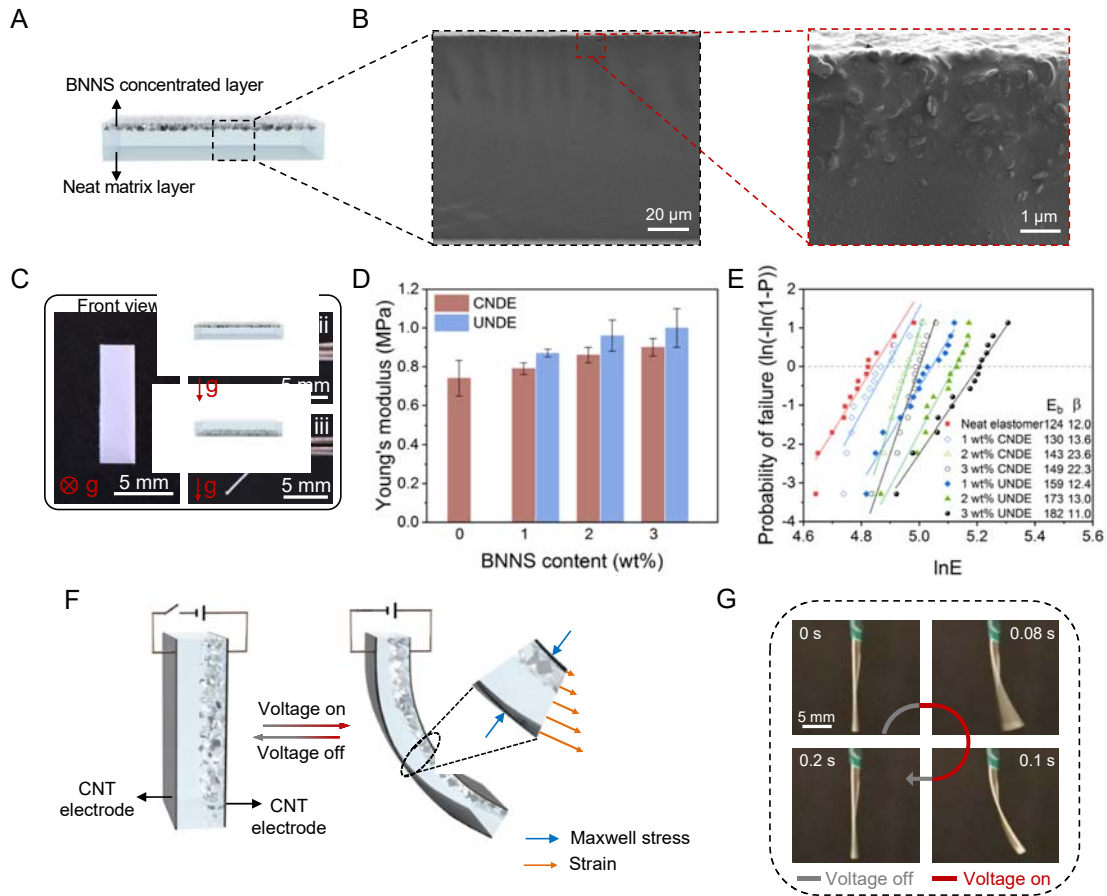**Structure characterization and bending mechanism of the UNDE film**

Fig. 2. Structural characterization and bending mechanism of the UNDE film. (**A**) Illustration of the cross-section of a UNDE film, with BNNS concentrated layer in its upper surface. (**B**) SEM images of the cross-section of UNDE with 3 wt% BNNS at two different magnifications. (**C**) Optical images of (i) top view of the UNDE film with 3 wt% BNNS laid on a bench, (ii) side view of the film clapped at one end with the BNNS concentrated layer on top and (iii) on bottom. (**D**) Young's modulus and (**E**) Weibull distribution of the breakdown field strength of a neat elastomer and CNDE and UNDE with different BNNS contents. (**F**) Bending actuation of the UNDE film toward the surface with concentrated BNNS in response to voltage application, and recovery to original shape when the voltage is removed. (**G**) Optical images of the side view of the 3 wt% UNDE during an actuation cycle (square wave with peak electric field of 19 MV/m at 5 Hz).

The UNDE structure fabricated after electrophoretic concentration and photocuring is displayed in Fig. 2A. The cross-section scanning electron microscope (SEM) images of the control conventional nanocomposite dielectric elastomer (CNDE) and the UNDE with 3 wt% BNNS are shown in Fig. S3 and Fig. 2B, respectively. In the CNDE, BNNS are homogeneously dispersed in the matrix, whereas after electrophoretic concentration, BNNS are distributed exclusively in a layer of ~ 3.1 µm close to the surface.

The UNDE film, horizontally held at one end with the BNNS concentrated layer on the top, displays a smaller bending curvature than when the BNNS concentrated layer is on the bottom (Fig. 2C). This indicates that the BNNS-concentrated layer is stiffer than the BNNS-depleted layer. The stiffness difference between the two layers is further evidenced with a tensile test (Fig. S4). The Young's modulus of the neat dielectric

elastomer film without BNNS is 0.74 MPa. The modulus of the CNDEs are slightly higher (Fig. 2D) due to the stress transfer from the polymer matrix to the BNNS. After electrophoretic concentration, the modulus of the UNDEs further increase. Typically, the modulus of 3 wt% UNDE comprising a 3.1 μm thick BNNS-concentrated layer and 102.9 μm thick pure DE layer is 1.0 MPa. The filler loading and Young's modulus of the 3.1 μm thick BNNS-concentrated layer are estimated to be 72 wt% and 9.63 MPa (Fig. S5), respectively, based on the relative thickness of the bilayer structure. In general, it is challenging to fabricate nanocomposites with high filler-loading which can contribute a power-law modulus increase (Fig. S5 and S6)(29).

The UNDE without interface between the stiff BNNS-concentrated layer and the soft neat DE matrix layer has clear advantages over other laminate structures fabricated with multiple steps (Fig. S7), and could be exploited to obtain bending actuation. To fabricate the unimorph actuators, single-walled carbon nanotubes (CNTs) were spray-coated onto both surfaces of the freestanding UNDE film as the compliant electrodes. A Weibull distribution of the breakdown field strength of the film was first measured. The result shown in Fig. 2E suggests that the breakdown strength (E_b) is improved in the UNDEs, i.e., from 124 MV/m of pure DE to 149 MV/m of the 3 wt% CNDE and further to 182 MV/m of the 3 wt% UNDE. The introduction of 3 wt% BNNS almost has no effect on the cross-linking structure of the DEs (Fig. S8), the largely enhanced field strength is likely due to the compact BNNS layer acting as an effective insulating barrier, blocking the development of electrical trees(26). The 3 wt% UNDE (Fig. S9) displays the lowest dielectric constant (ε_r = 4.96 @ 100 Hz) and suppressed dielectric loss (*tan δ* = 0.026 @ 100 Hz), compared to the neat dielectric elastomer (ε_r = 5.47 and *δ* = 0.053 @ 100 Hz) and 3 wt% CNDE (ε_r = 5.08 and *δ* = 0.034 @ 100 Hz).

When a high voltage is applied across the UNDE film, a bending actuation is immediately initiated. The actuation mechanism is illustrated in Fig. 2F. The applied electric field generates Maxwell stress, *p*, that compresses on the dielectric elastomer:

$$p = \varepsilon_r \varepsilon_0 E^2 \quad (1)$$

where ε_r is the material relative permittivity, ε_0 is the vacuum permittivity, and E is the electric field. Assuming a linear elasticity of the material in a small strain range, the transverse compressive strain, s_z, is expressed as:

$$s_z = -\frac{p}{Y} = -\frac{\varepsilon_r \varepsilon_0 E^2}{Y} \quad (2)$$

where Y is apparent Young's modulus of the compressed film. Since the volume of the elastomer does not change, the thickness reduction is shown as in-plane expansion in the x and y directions.

Specifically, the UNDE film can be analyzed with a two-layer model consisting of a BNNS concentrated layer and a neat matrix layer, and the properties in each layer can be assumed homogeneous. Thus, the electric field strength in each layer is inversely proportional to the dielectric constant when CNT electrodes are charged. Consequently, the electric field induced compressive strain ratio (*k*) of neat matrix layer and BNNS concentrated layer is expressed as:

$$k = \frac{s_{Z2}}{s_{Z1}} = \frac{Y_1 \, \varepsilon_{r1}}{Y_2 \, \varepsilon_{r2}} \quad (3)$$

where S_{z1} and S_{z2}, Y_1 and Y_2, and ε_{r1} and ε_{r2} are the compressive strain, Young's modulus, and dielectric constant of BNNS concentrated layer and neat matrix layer, respectively.

Since the BNNS-concentrated layer in the 3 wt% UNDE film has a much higher Young's modulus than the pure DE layer (9.63 MPa vs 0.74 MPa), and the dielectric constant of BNNS concentrated layer is estimated

to be larger than 4, because the dielectric constant of BNNS and neat matrix are 4 and 5.47 @ 100 Hz, respectively. The two layers possess very different $Y\varepsilon_r$. Upon application of an electric field, the two layers experience non-uniform compressive strains ($k > 9.5$), which effectively translates into a bending deformation towards the BNNS-concentrated side. When the electric field is removed and Maxwell stress is released, the UNDE film quickly recovers its original shape. A full cycle of the bending actuation and recovery is shown in Fig. 2G.
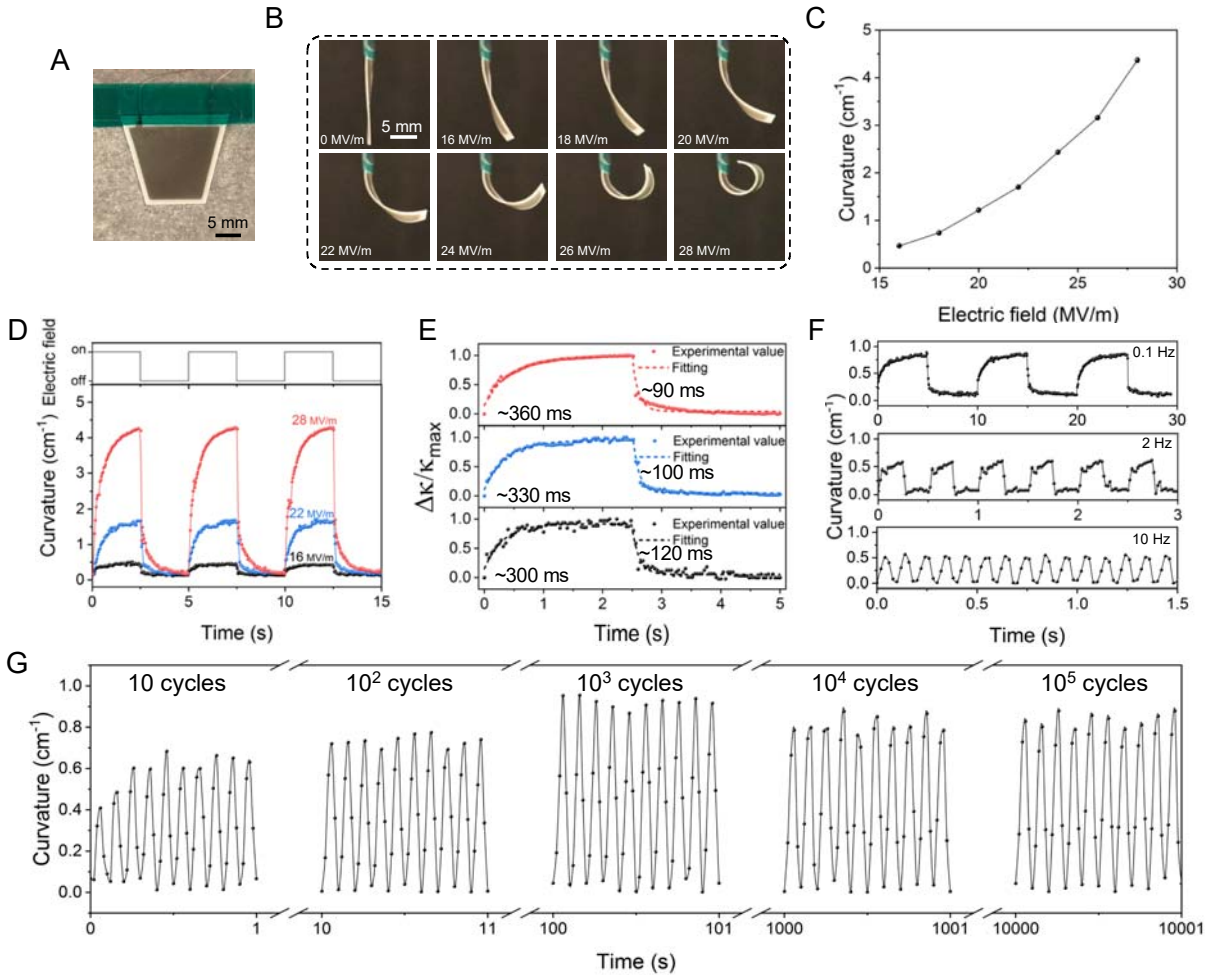
Bending actuation of the UNDE actuators

Fig. 3. Bending actuation performance of a 3 wt% UNDE actuator. (**A**) Photograph of a trapezoid-shaped UNDE actuator with 106 μm total thickness. (**B**) Side view images of the actuator at the specified electric fields. (**C**) Bending curvature plotted versus electric field. (**D**) Three consecutive waveforms of the applied electric field and the dynamic curvature responses at specified peak electric field. (**E**) Normalized curvature with time in one cycle from Fig. 3d to show the response time (63% curvature change) of the actuator when an electric field is applied and removed. (**F**) Bending curvature with time under square wave actuation at 0.1, 2, and 10 Hz with 19 MV/m peak electric field. (**G**) Bending actuation fatigue test under 21 MV/m peak electric field and 10 Hz in over 10,000 s of consecutive operation. The excerpted data demonstrate 1-10, 101-110, 1,001-1,010, 10,001-10,010, and 100,001-100,010 cycles.

A typical 3 wt% UNDE bending actuator is shown in Fig. 3A. The actuator is shaped in a trapezoid to suppress actuation at the corners. With one edge fixed to a rigid frame, the DEA actuates in a unidirectional bending manner in response to the applied electric fields across the thickness dimension (Fig. 3B). At a field intensity of 28 MV/m, a bending curvature of 4.4 cm^{-1} is achieved, resulting in an almost closed loop structure (Movie S1). The specific dependence of bending curvature on the electric field intensity is shown in Fig. 3C. UNDE with higher BNNS content requires higher electric field strength to achieve the same bending curvature (Fig. S10A) due to the stiffness increase, but it can produce larger blocked forces (Fig. S10B). Fig. 3D exhibits the recorded curvature values plotted as a function of time in three consecutive actuation cycles, under different applied field intensities at 0.2 Hz. Viscoelasticity of the dielectric elastomer results in a short delay when actuating between the two stationary states. The actuation and recovery processes can both be fitted with an exponential response using (*30*):

$$c = c_0 \left[1 - exp\left(-\frac{t}{\tau}\right)\right] \text{ for actuation} \qquad (4)$$

$$c = c_0 \, exp\left(-\frac{t}{\tau}\right) \text{ for recovery} \qquad (5)$$

where c_0 is the maximum stable bending curvature, t is time and τ is the response time constant. As shown in Fig. 3E, the response time constant of actuation is determined to be ~ 330 ms under three different field intensities (16, 22, and 28 MV/m); and the recovery time constant is calculated to be ~ 100 ms. The fast response of the bending DEA is attributed to the direct energy conversion from electricity to mechanical work, instead of relying on slower processes such as heat conduction, ionic migration, and solvent diffusion that occurred in unimorph actuators based on other mechanisms (Fig. S11 and Table S1)(*30-51*). The UNDE bending actuator displays uniform curvature changes in a wide range of operating frequencies from 0.1 to 10 Hz. (movie S2 and Fig. 3F). The specific dependence of curvature on operation frequency suggests that there is a trade-off between large bending curvature and high operation frequency, however, increasing the BNNS amount can broaden the bandwidth (Fig. S10C). The result of a continuous fatigue test of an actuator sample over 100,000 operating cycles under 21 MV/m and a frequency of 10 Hz is shown in Fig. 3G. After a short training process in the first 1,000 cycles, the repeated bending-induced strain could rearrange the existing reversible non-covalent bonds, i.e., hydrogen bonding(*52*), polymer chain entanglements, and other inter-polymer chain interactions.(*53*) Consequently, the stiffness of UNDE decreases during the training process and the bending curvature progressively improved from 0.4 to over 0.9 cm^{-1}; and this large deformation is preserved in the subsequent actuation cycles. Thanks to the interface-free feature between the passive BNNS concentrated layer and the active neat dielectric elastomer layer, the UNDE actuator display nondestructive bending performance after a 180° folding (Movie S2). It is worth noting that the electrophoretic concentration procedure is also applicable to silicone elastomers. The resulting actuator with a similar unimorph structure shows lower actuation curvatures and a wider bandwidth than acrylic elastomer due to their electromechanical differences (Fig. S12). Compared with ionic polymer metal composite (IPMC) actuator, the UNDE actuators shows superior performance in blocking force, curvature, response speed, and durability (Table S2)(*47-51, 54-56*).

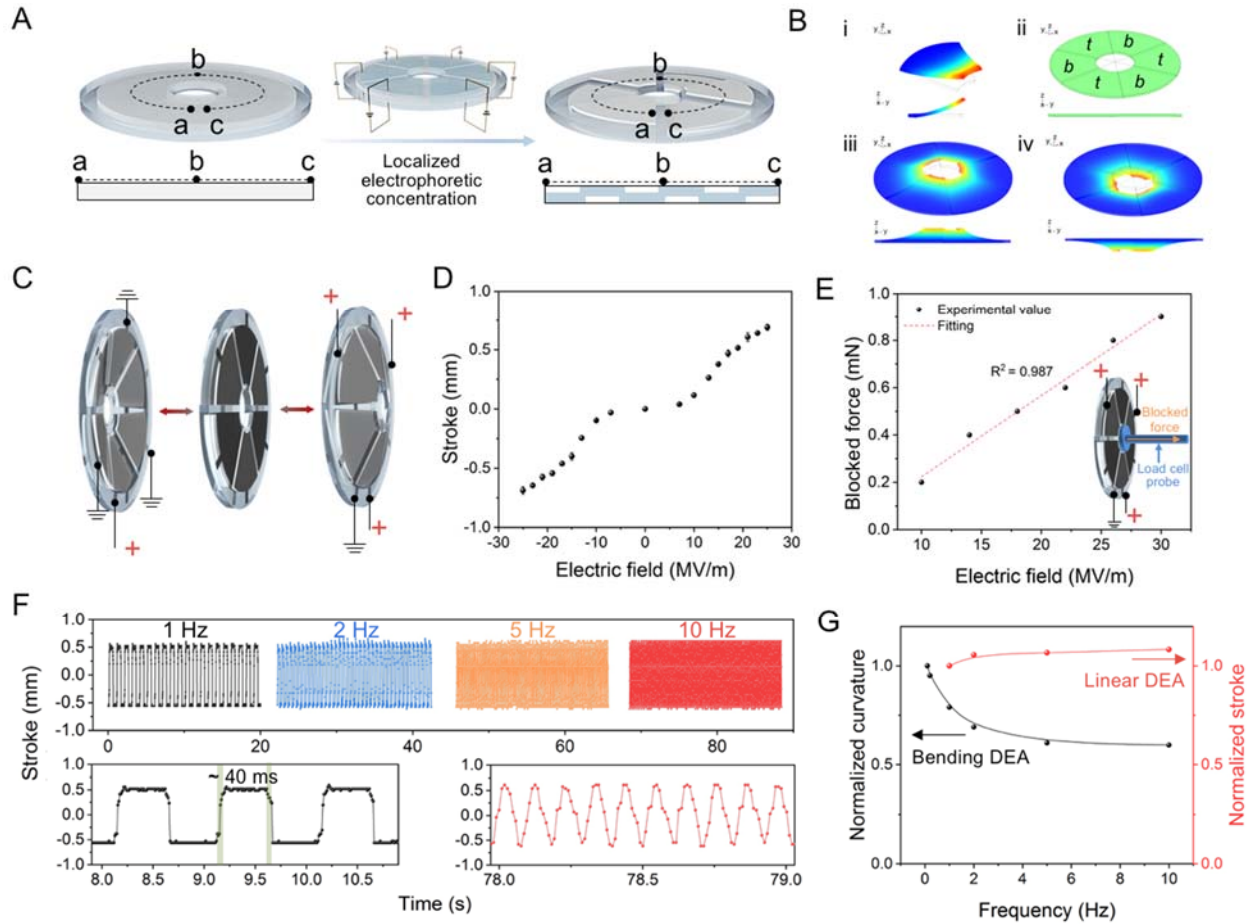**Disc-shaped linear DEA based on multiple UNDEs**

Fig. 4. **Structure of a disc-shaped linear DEA and its actuation performance**. (**A**) An illustration of a localized electrophoretic concentration process and the fabricated disc-shaped monolithic film with 6 BNNS concentrated sectors alternatively placed on the top and bottom surfaces; cross-sectional distribution of BNNS within the structure along the dashed line (a-b-c) are shown in the bottom. (**B**) Finite element analysis results on the actuation of a unimorph and a disc-shaped film with 6 unimorphs. (i) A single annular sector shaped unimorph with BNNS concentrated on the top surface bends upwards under an applied electric field. (ii) A simplified model of the disc-shaped monolithic film shown in Fig. 4A with BNNS alternately concentrated on the top (*t*) and bottom (*b*) surfaces. (iii) and (iv) the simplified model strokes up and down via application of electric fields across *t* and *b* regions, respectively. (**C**) A working principle diagram of a disc-shaped linear DEA. By separately applying a voltage to different actuator sections, a linear bidirectional stroke can be generated on the inner rim of the actuator. (**D**) Bidirectional stroke plotted versus electric field. (**E**) Blocking force of a disc-shaped linear DEA generated under different electric field strengths. (**F**) Bidirectional stroke under square wave actuation at 1, 2, 5, and 10 Hz with 19 MV/m peak electric field. Magnified view of several actuation cycles under 1 and 10 Hz are shown at the bottom. (**G**) Normalized curvature of a bending unimorph DEA and stroke of a disc-shaped linear DEA consisting of 6 unimorph units under 19 MV/m peak electric field at different actuation frequencies.

The UNDE fabrication process can be adapted to fabricate multiple individually accessible unimorphs integrated into a monolithic thin film. As a proof of concept, a soft disc-shaped actuator composed of 6 UNDE units was fabricated with a modified electrophoretic process (Fig. 4A and Fig. S13). To be specific,

BNNS in 6 annular sector regions were concentrated onto alternating surfaces (Fig. 4A) by applying electric fields in opposite directions among the adjacent localized regions. Both surfaces of the 6 UNDEs in the cured disc-shaped film were coated with CNT electrodes. When an electric field is applied to 3 functioning UNDE units with BNNS on the same surface, bending responses of the 3 charged sector regions collectively translate into an out-of-plane displacement at the inner rim (Fig. 4B). A bidirectional linear actuation of the film device is fulfilled by periodically triggering the two sets of UNDE units with voltages (Fig. S14 and Fig. 4C). A stable linear stroke generated upon application of certain voltage is shown in Fig. 4D, with symmetric linear strokes in either direction. At 25 MV/m, a unidirectional stroke of 0.69 mm is obtained, and the stroke combining the bidirectional motions is 1.38 mm, which is almost 4 times as large as the maximum stroke of 0.37 mm for the state-of-the-art commercial disc-shaped actuator made of multilayered piezoelectrics (57). Alternatively activating a half area of the disc-shaped film, the linear DEA understandably produces diluted blocked force which is linearly related to the electric field strength (Fig. 4E). Fig. 4F and Movie S3 indicate that the disc-shaped actuator operated under 19 MV/m performs the same stroke distance at 1, 2, 5, and 10 Hz, implying the displacement of this linear film DEA does not decrease with operational frequency up to 10 Hz, unlike the UNDE bending actuator whose bending curvature diminishes quickly with increasing frequency (Fig. 4G). Such a frequency-independent actuation performance is mainly contributed by the constrained small deformation and the antagonal mechanism in the disc-shaped DEA. Specifically, the disc-shaped actuator contains two sets of UNDE units, and delivers a bidirectional stroke by alternatively activating the two sets, meaning that only half the area of the disc-shaped film is activated while the other inactive half could constrain the actuation. As a result, the disc-shaped DEA generates a smaller deformation than a bending UNDE with a free end under the same electric field strength. Also, the response speed is enhanced from 150 ms via pure viscoelastic recovery to 40 ms via activation of one set of the UNDEs in sync with the recovery of the other set, thus vanquishing the material's viscoelasticity (Fig. S15). This large out-of-plane stroke, fast response, and stable DEA actuation was previously only obtained within multilayered structures (4) or relatively complex multi-component devices (58, 59).
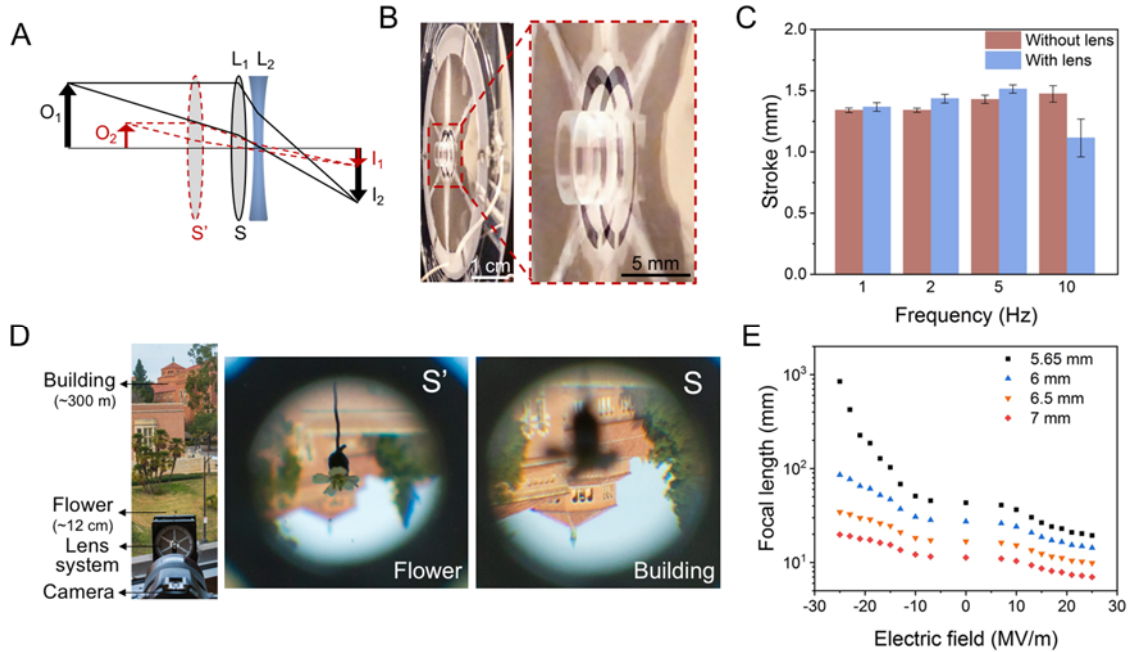
Compact and direct-drive lens motor

Fig. 5. **An optical zoom system driven by the disc-shaped linear DEA (lens motor)**. (**A**) Mechanism of an optical zoom system composed of a convex lens (L_1) and a concave lens (L_2). The focal length and the working distance of the system changes as L_1 moves from S to S'. (**B**) Double exposure images showing a convex lens (CAW110, Ø6.28 mm, 0.05 g) linearly driven by a lens motor by applying a 24 MV/m electric field. The lens is mounted to the inner rim of the motor via a pre-defined paper tape. (**C**) Stroke distance of a lens motor without and with the convex lens mounted to the inner rim. Bidirectional stroke under square wave actuation at 1, 2, 5, and 10 Hz with 24 MV/m peak electric field. (**D**) Left: photographic images showing the zoom system and objects at different distances; right: photographic images captured by the optical zoom system at two different focal lengths. (**E**) Focal length variation as a function of the initial distance between the two lenses and the electrical field applied.

The disc-shaped linear DEA was used as a self-contained lens motor to directly reposition an optical element and change the focal length of a compact and adaptive zoom lens system in a broad range. A schematic representation of a two-lens zoom system is shown in Fig. 5A. By increasing the distance between the two lenses, the system's focal length decreases, and objects from far to close working distances can be subsequently projected onto the same image plane. For electrically controlled zooming, the convex lens was mounted in the inner hollow space of the lens motor (Fig. S16). Unlike the commercial ultrasonic motors (USMs) that require extra components, such as gears, rotors, sliders to transform vibrations into linear movement that drives lenses. The disc-shaped lens motor can directly drive a convex lens along its optical axis (Fig. 5B), which allows the focusing unit to be made more compact, Fig. 5C compares the linear stroke of linear DEA with and without the lens mounted. Operating at 24 MV/m, the lens motor generates a stroke of ~ 1.4 mm, whose deviation is within 5% of the stroke by the motor without the lens mounted. The stroke holds quite well with operation frequencies from 1 to 5 Hz, but it declined by ~20% at 10 Hz. The center point of the lens drifted marginally (~ 50 μm) during the actuation under all frequencies (Fig. S17).

Fig. 5D left shows a specific setup of a zoom lens system consisting of the aspheric convex lens (f_1 = 10.92 mm) mounted in the center hollow space of the disc-shaped lens motor and a bi-concave lens (f_2 = -6.0 mm) placed 6.6 mm apart. The movement of the mounted convex lens effectively adjusts the distance between the two lenses, switching the working distance from a flower 12 cm away from the lens set to a building

structure 300 m from the system (Fig. 5D middle and right) at a frequency up to 5 Hz (Movie S4). As we reframe the up-side-down scene from the flower to the building, a 230% focal length increase from 9 mm to 30 mm was achieved, as is evidenced by a narrower angle of view and a higher degree of magnification. Importantly, the bidirectional actuation of the lens motor doubles the movement range of the mounted lens, without referring to an even higher driving voltage.

Depending on the initial lens distance, a 1.38 mm linear relative movement between the two lenses provided by the lens motor operating at 25 MV/m electric field can be translated into a wide range of focal length variation as shown in Fig. 5E. Specifically, a 40 times focal length change from 20 mm to 850 mm can be achieved with an initial lens distance of 5.65 mm. And this tuning can be controlled incrementally to cover the entire range of the plotted focusing dynamic range, if both lenses were driven by synchronized individual lens motors. Compared to tunable liquid lens technology, this linear actuator-driven optical zoom system achieves a greater focal length tuning capability (Table S3)(*60-65*), and minimizes the load during focus drive, which are desirable in devices such as endoscopes, smartphone cameras, virtual reality headsets, and machine vision systems.

DISCUSSION

In summary, a new approach has been developed to fabricate unimorph configuration in a monolith dielectric elastomer film. Electrophoresis was shown to be an effective technique to concentrate BNNS nanofillers in monomers which are subsequently cured to form an interface-free UNDE. The concentration of BNNS stiffens the surface layer of the dielectric elastomer film by more than 10 times, and suppresses the propagation of electrical treeing much more effectively than a uniform nanocomposite at the same BNNS loading(*26*). The UNDE film was bending actuated due to the non-uniform modulus in the z-direction. Several UNDE units were readily formed in a single DEA film by concentrating BNNS to designated surface areas. The disc-shaped DEA film incorporating 6 such UNDE sectors produced large and undecayed linear out-of-plane stroke up to 10 Hz. The bidirectional motion of 1.38 mm is 13 times as large as the film thickness. This linear DEA was thin (at 106 μm thickness) and versatile enough to fit in a compact lens system to drive an aspheric convex lens to obtain optical zooming with a wide focal length variation (> 40 times) at operational frequencies up to 5 Hz. Overall, the approach should prove beneficial in fabricating compact actuating device for robotic systems. In particular, the linear DEA could be promising for artificial robotic vision that seeks compact actuation solutions due to its customizability, scalability, and large stroke-thickness ratio. The operation frequency might be further enhanced by tuning the polymer viscoelasticity or further optimizing the device structure.

MATERIALS AND METHODS
Preparation of monomer solution

The DEA monomer solution is based on a formulation reported previously(*11, 52*).

Preparation of BNNS

BNNS was exfoliated from h-BN purchased from Shengyi Technology Co., Ltd. A mixture of 1 g h-BN, 40 g urea, and 16 ml deionized (DI) water was ball-milled at 500 rpm for 16 h, and the supernatant was collected after the product was diluted to 400 ml with DI water and centrifuged at 3,000 rpm for 30 min. The product was centrifuged at 8,000 rpm for 30 min to collect precipitation, diluted with 200 ml DI water, and bath sonicated for 1 h, these procedures were repeated three times to get a BNNS/water dispersion without residual urea. BNNS powder was collected by freeze-drying for 72 h.

Preparation of CNT solution

10 mg carbon nanotubes (P3-SWNT, Carbon Solution, Inc.) were dispersed in a mixed solvent of 18 ml isopropanol (IPA) and 2 ml DI water. The supernatant was collected after the solution was bath sonicated for 24 h and centrifuged at 7,500 rpm for 15 min.

Preparation of UNDE bending actuator

The as-prepared BNNS and monomer solutions were mixed and stirred overnight to form a uniform colloidal suspension containing 3 wt% of BNNS. An indium tin oxide (ITO) coated polyethylene terephthalate (PET) film was rendered hydrophilic by a UVO cleaner (144AX, Jelight Company Inc.) for 30 min, and a 5 wt% poly(acrylic acid)/water solution was spin-coated at 3,000 rpm for 60 s on the ITO surface to prepare a water-soluble sacrificial layer. The colloidal suspension was injected into an isosceles trapezoid-shaped (long base 18 mm x short base 10 mm x altitude 14.5 mm) mold with a thickness of 90 μm between the two as-prepared electrodes. An electric field (5 kV/mm) was applied across the electrodes for 40 min, after removing the electric field, the mixture was photo cross-linked with a UV light-curing equipment (Dymax ECE 5000) for 20 min, and post-cured by a Dymax ultraviolet curing conveyor equipped with a 2.5 W cm^{-2} Fusion 300S type 'H' ultraviolet curing bulb, at a speed of 6 feet per minute for one pass. The cured film was released from electrodes by immersion in DI water for 24 h. CNT solution was spray-coated onto both surfaces of the freestanding film through masks (long base 16 mm x short base 8 mm x altitude 11.5 mm). Conductive wires were connected onto the long base side of the CNT electrodes with carbon grease and fixed with polyester tapes.

Preparation of disc-shaped linear DEA

Two sets of ITO patterned on PET film (Fig. S18) was fabricated by etching with a pre-defined mask tape in a mixture solution of HCl (37%)/H$_2$O/HNO$_3$ (69%) with a volume ratio of 10:10:1, washing with DI water, and drying with a nitrogen gun. A water-soluble sacrificial layer was coated on the electrode with the same procedure mentioned in the previous paragraph. The colloidal suspension was injected into an annulus-shaped (outer diameter 53 mm, inner diameter 13 mm) mold with a thickness of 90 μm between two patterned ITO/PET. Electric fields (5 MV/m) with opposite directions were separately applied across the thickness dimension of two patterned regions for 40 min, and UV curing was subsequently conducted. A freestanding film was obtained with the same procedure mentioned in the previous paragraph, CNT solution was spray-coated on both surfaces of the film with pre-defined masks to fabricate compliant electrodes for the disc-shaped DEA. The disc-shaped DEA was mounted on two ring-shaped PET frames (outer diameter 63 mm, inner diameter 50 mm, each 100 μm thick). Silver paste traces were printed on the PET frames before the mounting.

Electrophoretic kinetics characterization

A colloidal suspension containing 3 wt% BNNS was injected into a customized PDMS cuvette (length 2.5 mm x width 0.3 mm x height 1 mm) with parallel ITO electrodes on the top and bottom sides. A light source was set behind the cuvette to supply a beam of incident light. Different electric fields (0, 3, 4, and 5 MV/m) were applied across the two electrodes. A digital camera (Canon 70D) was used to record the light intensity after transmitting the cuvette by shooting videos. Pictures exported from videos by the time were transmitted into grayscale to evaluate light intensity with the equation:

$$grayscale = R \times 0.299 + G \times 0.587 + B \times 0.144 \quad (6)$$

Where R, G, and B are the RGB values of the exported pictures. To calibrate grayscale readings against known mass concentrations of the suspended BNNS in monomer solution, grayscale values of colloidal solutions with certain BNNS concentrations (0.03, 0.09, 0.15, 0.95, and 3 wt%) were acquired with the

same method. As the incident light beam is scattered due to the presence of the suspending BNNS. The attenuated transmitted light intensity can be described with the function (28):

$$I = I_0 e^{-\tau l} \qquad (7)$$

where I_0 is the incident light intensity, I is the light intensity after passing through a medium of length l, and τ is the turbidity coefficient of the medium, which is proportional to the concentration of the dispersed BNNS. Given the transmitted light intensity is proportional to the grayscale values, the fitting correlation between grayscale and BNNS concentration is obtained with an exponential function.

SEM characterization

The CNDE and UNDE films were freeze fractured in liquid nitrogen to acquire cross-section surfaces, and the surfaces were sputter-coated with gold. The dispersion and distribution of BNNS in both composites were characterized with a field emission scanning electron microscope (FESEM, ZEISS Supra 40VP) at an accelerating voltage of 3 kV.

TEM characterization

The freeze-dried BNNS were dispersed in a mixture solution of IPA/H_2O (volume ratio of 1:1). After a 30 min sonication, 20 µl of the suspension was drop cast onto a copper grid, and the sample was characterized with a transmission electron microscopy (TEM, T12 Quick CryoEM) after complete drying.

Mechanical property characterization

The uniaxial tensile fracture test was performed on a dynamic mechanical analyzer (DMA, TA RSA III) with a crosshead speed of 0.05 mm/s at room temperature. At least five dumb-bell samples with a dimension of 10 mm × 3 mm × 0.1 mm were repeatedly tested and average results were reported.

Breakdown and dielectric property characterization

Dielectric breakdown strength was measured under a DC voltage ramp of 500 V/s supplied by a hi-pot tester (957i Vitrek). At least 15 samples were measured for each test. The frequency-dependent dielectric constant and loss were measured by an LCR meter (GwInstek LCR-819) from 12 Hz to 10^4 Hz.

Bending actuation characterization

The UNDE bending actuator was vertically mounted on a grip. Conductive wires attached to the compliant electrodes were connected to a high-voltage power source (10/10B-HS, Trek). The bending actuation in response to square wave voltage signals was recorded using the digital camera. Videos were subjected to frame-wise analysis to determine bending curvatures.

Linear actuation characterization

The disc-shaped linear DEA mounted on PET frames was vertically hold. Printed silver paste attached to the compliant electrodes was connected to a circuit (Fig. S14) controlling voltages supplied by the high-voltage power source. The out-of-plane actuation in response to voltage signals was recorded by shooting videos at 120 fps, and videos were subjected to frame-wise analysis to extract displacements of the inner rim.

Finite element analysis

A simulation of the Disc-shaped linear DEA based on multiple UNDEs was carried out in COMSOL Multiphysics. An electrostatics (electrostriction) module was coupled with the solid mechanics module to

simulate the dielectric actuation process. The three parameter Mooney-Rivlin model was chosen to model the hyperelasticity of the two layers of UNDEs. The material parameters were based on the measured materials properties (modulus, density, etc).

Lens motor and optical zoom lens system characterization

A plastic aspheric convex lens (CAW110, Ø6.28 mm, f_1 = 10.92 mm, Thorlabs, Inc.) was mounted in the inner circle part of the disc-shaped DEA with a pre-defined paper tape. The disc-shaped DEA was operated under square wave actuation at 1, 2, 5, and 10 Hz with a 24 MV/m peak electric field. The motion trail of the lens was recorded by the phone camera. The stroke distance and center drift of the lens center were measured by video frame-wise analysis. The zoom lens system was set up with the convex lens mounted lens motor and a Bi-concave lens (LD2746, Ø6 mm, f_2 = -6.0 mm, Thorlabs, Inc.), with a lens separation of 6.6 mm. The digital camera with a macro lens (EF 100mm f/2.8L Macro IS USM) was 300 mm away from the lens set for object image recording. The lens motor was activated under square wave actuation at 1, 2, 5, and 10 Hz with a 24 MV/m peak electric field to regularly change the lens distance. The dynamic inverted real images produced by the zoom lens system were continuously recorded by the digital camera. We calculated the back focal length (*b. f. l.*) variation of the two-lens zoom system driven by the lens motor under different electric fields using the two-lens equation:

$$b.f.l. = \frac{f_2(d-f_1)}{d-(f_1+f_2)} \quad (8)$$

where f_2 and f_1 are the focal length of the concave lens and convex lens, respectively, d is the distance between two lenses.

SUPPLEMENTARY MATERIALS

Fig. S1. BNNS and colloidal dispersion.

Fig. S2. Kinetic study of the electrophoretic concentration process.

Fig. S3. SEM images of the cross-section of the 3 wt% CNDE.

Fig. S4. Stress-strain curves of a neat elastomer and CNDE and UNDE with different BNNS contents.

Fig. S5. Young's modulus of CNDEs with 10, 20, and 30 wt% BNNS fabricated by directly mixing method and the concentrated 72 wt% BNNS layer in 3 wt% UNDE.

Fig. S6. Fabrication of high-loading nanocomposite by directly mixing BNNS and monomers.

Fig. S7. Laminate structures fabricated via conventional multi-step methods and electrophoretic concentration studied in this report.

Fig. S8. Gel content of the cross-linked neat elastomer, 3 wt% CNDE, and 3 wt% UNDE.

Fig. S9. Dielectric constant and tan δ of a neat elastomer, CNDEs and UNDEs containing 1, 2 and 3 wt% BNNS.

Fig. S10. Bending actuation performance of UNDE actuators with 1, 2, and 3 wt% BNNS.

Fig. S11. The figure of merit actuation performance (curvature × thickness vs. response time) of important polymer thin film bending actuators.

Fig. S12. Structure and performance of 3 wt% Silicone-UNDE bending actuator.

Fig. S13. A disc-shaped linear DEA.

Fig. S14. Circuit and electric field waveforms employed to power the disc-shaped DEA with two actuator sets (AS$_1$ and AS$_2$).

Fig. S15. The electric field waveforms applied on a disc-shaped DEA with two UNDE sets and the generated stroke.

Fig. S16. A photograph of lens motor.

Fig. S17. Central drift of a lens driven by a disc-shaped actuator.

Fig. S18. A diagram of electrode for localized electrophoretic concentration to make the disc-shaped linear actuators.

Table S1. Performance comparison of photo-thermal, electro-thermal, solvent, electro-chemical, and electric field stimulated film bending actuators.

Table S2. performance comparison of IPMC and UNDE bending actuators with similar dimensions.

Table S3. Size and performance comparison of tunable lenses using DEAs.

Movie S1. Closed loop bending of a UNDE actuator.

Movie S2. Durable bending actuation of a UNDE actuator after folding.

Movie S3. Bending at different frequencies of a UNDE actuator.

Movie S4. Linear stroke at different frequencies of a disc-shaped DEA.

Movie S5. Working distances change at different frequencies of an optical zoom system driven by the disc-shaped linear DEA.

REFERENCES

1.   R. Pelrine, R. Kornbluh, Q. B. Pei, J. Joseph, High-speed electrically actuated elastomers with strain greater than 100%. *Science* **287**, 836-839 (2000).
2.   P. Brochu, Q. Pei, Advances in dielectric elastomers for actuators and artificial muscles. *Macromol Rapid Commun.* **31**, 10-36 (2010).
3.   Y. Chen, H. Zhao, J. Mao, P. Chirarattananon, E. F. Helbling, N.-s. P. Hyun, D. R. Clarke, R. J. Wood, Controlled flight of a microrobot powered by soft artificial muscles. *Nature* **575**, 324-329 (2019).
4.   M. Duduta, E. Hajiesmaili, H. Zhao, R. J. Wood, D. R. Clarke, Realizing the potential of dielectric elastomer artificial muscles. *Proc. Natl. Acad. Sci. U.S.A.* **116**, 2476-2481 (2019).
5.   G. Li, X. Chen, F. Zhou, Y. Liang, Y. Xiao, X. Cao, Z. Zhang, M. Zhang, B. Wu, S. Yin, Y. Xu, H. Fan, Z. Chen, W. Song, W. Yang, B. Pan, J. Hou, W. Zou, S. He, X. Yang, G. Mao, Z. Jia, H. Zhou, T. Li, S. Qu, Z. Xu, Z. Huang, Y. Luo, T. Xie, J. Gu, S. Zhu, W. Yang, Self-powered soft robot in the Mariana Trench. *Nature* **591**, 66-71 (2021).
6.   X. Ji, X. Liu, V. Cacucciolo, M. Imboden, Y. Civet, A. El Haitami, S. Cantin, Y. Perriard, H. Shea, An autonomous untethered fast soft robotic insect driven by low-voltage dielectric elastomer actuators. *Sci. Robot.* **4**, eaaz6451 (2019).

7. X. Niu, P. Brochu, H. Stoyanov, S. R. Yun, Q. Pei, Bistable electroactive polymer for refreshable Braille display with improved actuation stability. *Proc. SPIE*, **8340**, 83400R (2012).
8. X. Ji, X. Liu, V. Cacucciolo, Y. Civet, A. El Haitami, S. Cantin, Y. Perriard, H. Shea, Untethered Feel‐Through Haptics Using 18‐μm Thick Dielectric Elastomer Actuators. *Adv. Funct. Mater.* **31**, 2006639 (2021).
9. P. Sommer-Larsen, G. Kofod, M. Shridhar, M. Benslimane, P. Gravesen, Performance of dielectric elastomer actuators and materials. *Proc. SPIE*, **4695**, 158 (2002)
10. S. M. Ha, W. Yuan, Q. Pei, R. Pelrine, S. Stanford, Interpenetrating Polymer Networks for High-Performance Electroelastomer Artificial Muscles. *Adv. Mater.* **18**, 887-891 (2006).
11. X. Niu, H. Stoyanov, W. Hu, R. Leo, P. Brochu, Q. Pei, Synthesizing a new dielectric elastomer exhibiting large actuation strain and suppressed electromechanical instability without prestretching. *J. Polym. Sci. B Polym. Phys.* **51**, 197-206 (2013).
12. P. H. Vargantwar, A. E. Özçam, T. K. Ghosh, R. J. Spontak, Prestrain-Free Dielectric Elastomers Based on Acrylic Thermoplastic Elastomer Gels: A Morphological and (Electro)Mechanical Property Study. *Adv. Funct. Mater.* **22**, 2100-2113 (2012).
13. Y. Yang, Z.-S. Gao, M. Yang, M.-S. Zheng, D.-R. Wang, J.-W. Zha, Y.-Q. Wen, Z.-M. Dang, Enhanced energy conversion efficiency in the surface modified BaTiO3 nanoparticles/polyurethane nanocomposites for potential dielectric elastomer generators. *Nano Energy* **59**, 363-371 (2019).
14. G. Gallone, F. Carpi, D. De Rossi, G. Levita, A. Marchetti, Dielectric constant enhancement in a silicone elastomer filled with lead magnesium niobate–lead titanate. *Mater. Sci. Eng. C* **27**, 110-116 (2007).
15. H. Stoyanov, M. Kollosche, S. Risse, D. N. McCarthy, G. Kofod, Elastic block copolymer nanocomposites with controlled interfacial interactions for artificial muscles with direct voltage control. *Soft Matter* **7**, 194-202 (2011).
16. W. Hu, S. N. Zhang, X. Niu, C. Liu, Q. Pei, An aluminum nanoparticle–acrylate copolymer nanocomposite as a dielectric elastomer with a high dielectric constant. *J. Mater. Chem. C* **2**, 1658-1666 (2014).
17. Z. S. Davidson, H. Shahsavan, A. Aghakhani, Y. Guo, L. Hines, Y. Xia, S. Yang, M. Sitti, Monolithic shape-programmable dielectric liquid crystal elastomer actuators. *Sci. Adv.* **5**, eaay0855 (2019).
18. S. Shian, K. Bertoldi, D. R. Clarke, Dielectric Elastomer Based "Grippers" for Soft Robotics. *Adv. Mater.* **27**, 6814-6819 (2015).
19. T. Li, G. Li, Y. Liang, T. Cheng, J. Dai, X. Yang, B. Liu, Z. Zeng, Z. Huang, Y. Luo, T. Xie, W. Yang, Fast-moving soft electronic fish. *Sci. Adv.* **3**, e1602045 (2017).
20. G. Kovacs, L. Düring, S. Michel, G. Terrasi, Stacked dielectric elastomer actuator for tensile force transmission. *Sens. Actuator A Phys.* **155**, 299-307 (2009).
21. C. Tugui, M.-S. Serbulea, M. Cazacu, Preparation and characterisation of stacked planar actuators. *Chem. Eng. Sci.* **364**, 217-225 (2019).
22. M. Duduta, R. J. Wood, D. R. Clarke, Multilayer Dielectric Elastomers for Fast, Programmable Actuation without Prestretch. *Adv. Mater.* **28**, 8058-8063 (2016).
23. J. Shintake, S. Rosset, B. Schubert, D. Floreano, H. Shea, Versatile Soft Grippers with Intrinsic Electroadhesion Based on Multifunctional Polymer Actuators. *Adv. Mater.* **28**, 231-238 (2016).
24. B. Aksoy, H. Shea, Reconfigurable and Latchable Shape-Morphing Dielectric Elastomers Based on Local Stiffness Modulation. *Adv. Funct. Mater.* **30**, 2001597 (2020).
25. J. Shintake, V. Cacucciolo, H. Shea, D. Floreano, Soft Biomimetic Fish Robot Made of Dielectric Elastomer Actuators. *Soft Robot.* **5**, 466-474 (2018).
26. Y. Zhu, Y. Zhu, X. Huang, J. Chen, Q. Li, J. He, P. Jiang, High Energy Density Polymer Dielectrics Interlayered by Assembled Boron Nitride Nanosheets. *Adv. Energy Mater.* **9**, 1901826 (2019).

27. W. Lei, V. N. Mochalin, D. Liu, S. Qin, Y. Gogotsi, Y. Chen, Boron nitride colloidal solutions, ultralight aerogels and freestanding membranes through one-step exfoliation and functionalization. *Nat. Commun.* **6**, 8849 (2015).

28. D. M. Lawler, "SPECTROPHOTOMETRY | Turbidimetry and Nephelometry" in *Encyclopedia of Analytical Science (Second Edition),* P. Worsfold, A. Townshend, C. Poole, Eds. (Elsevier, Oxford, 2005), pp. 343-351.

29. D. W. Schaefer, R. S. Justice, How Nano Are Nanocomposites? *Macromolecules* **40**, 8501-8517 (2007).

30. X. Zhang, Z. Yu, C. Wang, D. Zarrouk, J. W. Seo, J. C. Cheng, A. D. Buchan, K. Takei, Y. Zhao, J. W. Ager, J. Zhang, M. Hettick, M. C. Hersam, A. P. Pisano, R. S. Fearing, A. Javey, Photoactuators and motors based on carbon nanotubes with selective chirality distributions. *Nat. Commun.* **5**, 2983 (2014).

31. J. Li, R. Zhang, L. Mou, M. Jung de Andrade, X. Hu, K. Yu, J. Sun, T. Jia, Y. Dou, H. Chen, S. Fang, D. Qian, Z. Liu, Photothermal Bimorph Actuators with In-Built Cooler for Light Mills, Frequency Switches, and Soft Robots. *Adv. Funct. Mater.* **29**, 1808995 (2019).

32. S. Wang, Y. Gao, A. Wei, P. Xiao, Y. Liang, W. Lu, C. Chen, C. Zhang, G. Yang, H. Yao, T. Chen, Asymmetric elastoplasticity of stacked graphene assembly actualizes programmable untethered soft robotics. *Nat. Commun.* **11**, 4359 (2020).

33. J. Deng, J. Li, P. Chen, X. Fang, X. Sun, Y. Jiang, W. Weng, B. Wang, H. Peng, Tunable Photothermal Actuators Based on a Pre-programmed Aligned Nanostructure. *J. Am. Chem. Soc.* **138**, 225-230 (2016).

34. H. Kim, H. Lee, I. Ha, J. Jung, P. Won, H. Cho, J. Yeo, S. Hong, S. Han, J. Kwon, K.-J. Cho, S. H. Ko, Biomimetic Color Changing Anisotropic Soft Actuators with Integrated Metal Nanowire Percolation Network Transparent Heaters for Soft Robotics. *Adv. Funct. Mater.* **28**, 1801847 (2018).

35. J. Ahn, Y. Jeong, Z.-J. Zhao, S. Hwang, K. Kim, J. Ko, S. Jeon, J. Park, H. Kang, J.-H. Jeong, I. Park, Heterogeneous Conductance-Based Locally Shape-Morphable Soft Electrothermal Actuator. *Adv. Mater. Technol.* **5**, 1900997 (2020).

36. Z. Zeng, H. Jin, L. Zhang, H. Zhang, Z. Chen, F. Gao, Z. Zhang, Low-voltage and high-performance electrothermal actuator based on multi-walled carbon nanotube/polymer composites. *Carbon* **84**, 327-334 (2015).

37. Y. Hu, T. Lan, G. Wu, Z. Zhu, W. Chen, A spongy graphene based bimorph actuator with ultra-large displacement towards biomimetic application. *Nanoscale* **6**, 12703-12709 (2014).

38. Q. Li, C. Liu, Y.-H. Lin, L. Liu, K. Jiang, S. Fan, Large-Strain, Multiform Movements from Designable Electrothermal Actuators Based on Large Highly Anisotropic Carbon Nanotube Sheets. *ACS Nano* **9**, 409-418 (2015).

39. Y. Dong, J. Wang, X. Guo, S. Yang, M. O. Ozen, P. Chen, X. Liu, W. Du, F. Xiao, U. Demirci, B.-F. Liu, Multi-stimuli-responsive programmable biomimetic actuator. *Nat. Commun.* **10**, 4087 (2019).

40. J. Cao, Z. Zhou, Q. Song, K. Chen, G. Su, T. Zhou, Z. Zheng, C. Lu, X. Zhang, Ultrarobust Ti_3C_2Tx MXene-Based Soft Actuators via Bamboo-Inspired Mesoscale Assembly of Hybrid Nanostructures. *ACS Nano* **14**, 7055-7065 (2020).

41. Y. Liu, B. Xu, S. Sun, J. Wei, L. Wu, Y. Yu, Humidity- and Photo-Induced Mechanical Actuation of Cross-Linked Liquid Crystal Polymers. *Adv. Mater.* **29**, 1604792 (2017).

42. B. Shin, J. Ha, M. Lee, K. Park, H. Park Gee, H. Choi Tae, K.-J. Cho, H.-Y. Kim, Hygrobot: A self-locomotive ratcheted actuator powered by environmental humidity. *Sci. Robot.* **3**, eaar2629 (2018).

43. M. Acerce, E. K. Akdoğan, M. Chhowalla, Metallic molybdenum disulfide nanosheet-based electrochemical actuators. *Nature* **549**, 370-373 (2017).

44. K. Li, Y. Shao, H. Yan, Z. Lu, K. J. Griffith, J. Yan, G. Wang, H. Fan, J. Lu, W. Huang, B. Bao, X. Liu, C. Hou, Q. Zhang, Y. Li, J. Yu, H. Wang, Lattice-contraction triggered synchronous electrochromic actuator. *Nat. Commun.* **9**, 4798 (2018).

45. L. Ji, Y. Yu, Q. Deng, S. Shen, Tailoring the nanostructures of electrochemical actuators for fast response and large deformation. *Nanoscale* **12**, 15643-15651 (2020).

46. I. S. Romero, N. P. Bradshaw, J. D. Larson, S. Y. Severt, S. J. Roberts, M. L. Schiller, J. M. Leger, A. R. Murphy, Biocompatible Electromechanical Actuators Composed of Silk-Conducting Polymer Composites. *Adv. Funct. Mater.* **24**, 3866-3873 (2014).

47. J. H. Park, S. W. Lee, D. S. Song, J. Y. Jho, Highly Enhanced Force Generation of Ionic Polymer–Metal Composite Actuators via Thickness Manipulation. *ACS Appl. Mater. Interfaces* **7**, 16659-16667 (2015).

48. S. Liu, Y. Liu, H. Cebeci, R. G. de Villoria, J.-H. Lin, B. L. Wardle, Q. M. Zhang, High Electromechanical Response of Ionic Polymer Actuators with Controlled-Morphology Aligned Carbon Nanotube/Nafion Nanocomposite Electrodes. *Adv. Funct. Mater.* **20**, 3266-3271 (2010).

49. C. Lu, Y. Yang, J. Wang, R. Fu, X. Zhao, L. Zhao, Y. Ming, Y. Hu, H. Lin, X. Tao, Y. Li, W. Chen, High-performance graphdiyne-based electrochemical actuators. *Nat. Commun.* **9**, 752 (2018).

50. G. Wu, Y. Hu, Y. Liu, J. Zhao, X. Chen, V. Whoehling, C. Plesse, G. T. M. Nguyen, F. Vidal, W. Chen, Graphitic carbon nitride nanosheet electrode-based high-performance ionic actuator. *Nat. Commun.* **6**, 7258 (2015).

51. M. Kotal, J. Kim, K. J. Kim, I.-K. Oh, Sulfur and Nitrogen Co-Doped Graphene Electrodes for High-Performance Ionic Artificial Muscles. *Adv. Mater.* **28**, 1610-1615 (2016).

52. W. Hu, X. Niu, X. Yang, N. Zhang, Q. Pei, Synthesis and electromechanical characterization of a new acrylic dielectric elastomer with high actuation strain and dielectric strength. *Proc. SPIE* **8687**, 86872U (2013).

53. Y. Chen, G. Kang, J. Yuan, T. Li, Experimental study on pure-shear-like cyclic deformation of VHB 4910 dielectric elastomer. *J. Polym. Res.* **26**, 186 (2019).

54. M. C. Saccardo, A. G. Zuquello, K. A. Tozzi, R. Gonçalves, L. A. Hirano, C. H. Scuracchio, Counter-ion and humidity effects on electromechanical properties of Nafion®/Pt composites. *Mater. Chem. Phys.* **244**, 122674 (2020).

55. J. Kim, S.-H. Bae, M. Kotal, T. Stalbaum, K. J. Kim, I.-K. Oh, Soft but Powerful Artificial Muscles Based on 3D Graphene–CNT–Ni Heteronanostructures. *Small* **13**, 1701314 (2017).

56. S. Imaizumi, Y. Ohtsuki, T. Yasuda, H. Kokubo, M. Watanabe, Printable Polymer Actuators from Ionic Liquid, Soluble Polyimide, and Ubiquitous Carbon Materials. *ACS Appl. Mater. Interfaces* **5**, 6307-6315 (2013).

57. Ring bender, CMBR07, http://www.noliac.com/products/actuators/ring-benders/show/cmbr07/. (2021).

58. E. Acome, S. K. Mitchell, T. G. Morrissey, M. B. Emmett, C. Benjamin, M. King, M. Radakovitz, C. Keplinger, Hydraulically amplified self-healing electrostatic actuators with muscle-like performance. *Science* **359**, 61-65 (2018).

59. I. D. Sîrbu, G. Moretti, G. Bortolotti, M. Bolignari, S. Diré, L. Fambri, R. Vertechy, M. Fontana, Electrostatic bellow muscle actuators and energy harvesters that stack up. *Sci. Robot.* **6**, eaaz5796 (2021).

60. F. Carpi, G. Frediani, S. Turco, D. De Rossi, Bioinspired Tunable Lens with Muscle-Like Electroactive Elastomers. *Adv. Funct. Mater.* **21**, 4152-4158 (2011).

61. S. Shian, R. M. Diebold, D. R. Clarke, Tunable lenses using transparent dielectric elastomer actuators. *Opt. Express* **21**, 8669-8676 (2013).

62. L. Maffli, S. Rosset, M. Ghilardi, F. Carpi, H. Shea, Ultrafast All-Polymer Electrically Tunable Silicone Lenses. *Adv. Funct. Mater.* **25**, 1656-1665 (2015).

63. M. Pieroni, C. Lagomarsini, D. De Rossi, F. Carpi, Electrically tunable soft solid lens inspired by reptile and bird accommodation. *Bioinspir. Biomim.* **11**, 065003 (2016).

64. S. Nam, S. Yun, J. W. Yoon, S. Park, S. K. Park, S. Mun, B. Park, K.-U. Kyung, A Robust Soft Lens for Tunable Camera Application Using Dielectric Elastomer Actuators. *Soft Robot.* **5**, 777-782 (2018).

65. Y. Wang, P. Li, U. Gupta, J. Ouyang, J. Zhu, Tunable Soft Lens of Large Focal Length Change. *Soft Robot.* doi.org/10.1089/soro.2021.0036 (2021).